

Blazar boosted Dark Matter - direct detection constraints on $\sigma_{e\chi}$: Role of energy dependent cross sections

Supritha Bhowmick,^{1,*} Diptimoy Ghosh,^{1,†} and Divya Sachdeva^{2,‡}

¹*Department of Physics, Indian Institute of Science Education and Research Pune, India*

²*Laboratoire de Physique de l'Ecole Normale Supérieure, CNRS,
Université PSL, Sorbonne Universités, 24 rue Lhomond, 75005 Paris, France*

Elastic collisions with relativistic electrons from the blazar's jet can accelerate dark matter (DM) particles in the DM spike surrounding the supermassive black hole at its center. This can allow one to set stringent limits on the DM-electron scattering cross section ($\bar{\sigma}_{e\chi}$) for DM masses less than 100 MeV. We consider DM particles boosted by energetic electrons in the jets of the blazars TXS 0506+056 and BL Lacertae. Both vector and scalar mediators for the scattering of electron and electrophilic fermionic DM are studied. We highlight that the ensuing energy dependence of the S-matrix for the corresponding Lorentz structure of the vertex significantly modifies the constraints. We find that the revised exclusion limits are orders of magnitude stronger than the equivalent results for the simple constant cross section assumption. Our limits are also assessed for the less cuspy spike.

I. INTRODUCTION

The Cold Dark Matter (CDM) provides a compelling explanation for a broad range of observations, including rotation curves in spiral galaxies, gravitational microlensing, cluster collisions (the Bullet Cluster), and temperature anisotropy in the spectrum of cosmic microwave background radiation. To that end, a variety of particle physics models predict a feeble interaction between SM and DM, which can be investigated using Direct detection (DD) experiments. The DD experiments identify the nuclear or electronic recoils produced by the scattering between DM and the detector's (target) nuclei or electrons. The average velocity of DM particles in the solar vicinity, however, restricts the amount of energy that may be deposited in a detector. For example: detectors like XENON1T can detect DM mass $m_\chi \sim \mathcal{O}(1 \text{ MeV})$, corresponding to electronic recoil of $\sim \mathcal{O}(1 \text{ keV})$ [1]. The neutrino detectors like SUPER-K are sensitive to recoil energy threshold of $\sim \mathcal{O}(1 \text{ MeV})$ [2, 3] leading to the smallest accessible DM mass of $\mathcal{O}(1 \text{ GeV})$ ¹. Thus, these detectors appear to have a limited range for detecting lighter DM particles. Since these observations have been unfavourable towards confirmed detection of DM, it is critical to develop methods for probing the sub-GeV/MeV mass range.

The reach of these experiments has been extended to DM masses well below 1 GeV in recent years, thanks to the novel idea of boosting the halo DM through its interaction with the SM particles via cosmic rays [7–24], primordial black holes [25, 26], diffuse Supernova Neutrino Background (DSNB) [14–18], and blazars [27, 28]. Even

though the boosted DM flux is substantial and DM particles are (semi)relativistic, the population of the up-scattered subcomponent of DM is significantly lower than the galactic DM population. Hence sensitivity for boosted DM is achieved at cross sections much larger than unboosted scenario.

In this paper, we consider the blazar boosted DM, which was proposed in Ref. [27, 28] in the context of fermionic DM. The presence of a supermassive Black Hole (BH) at the blazar center, which provides a dense DM population compensates for the blazar's large distance from Earth by producing DM flux that is stronger than that from galactic CRs. The existing literature, however, assumes that DM interaction cross-sections are independent of DM energy. Although this simple assumption makes calculations easier, it's not physically realistic. It would also be an incorrect approximation to make, notably in scenarios where a significant DM flux becomes relativistic after being scattered by energetic particles. Some of the previously mentioned works [11, 20–22, 29] for cosmic ray boosted DM, have already discovered that the limits for energy-dependent cross-section differ by orders of magnitude from those obtained under the assumption of a constant cross section.

The notion of an energy-dependent scattering cross-section is thus primarily investigated in the present work by taking into account electrophilic fermionic DM that has been boosted by energetic electrons from blazars. To constrain the scattering cross-section, we use electron recoil measurements in Super-Kamiokande. This work is organized as follows. We discuss the spectrum of energetic particles in the blazar jets in Section II, and describe DM density profiles in Section III. In Section IV, we estimate the Blazar boosted DM (BBDM) flux and compute the event rate. In Section V, we present simplified DM models. We present the main results of our paper in Section VI, i.e., the energy dependent exclusion bound from BBDM-electron scattering, and in Section VII, we summarize and conclude.

* supritha.bhowmick@students.iiserpune.ac.in

† diptimoy.ghosh@iiserpune.ac.in

‡ divya.sachdeva@phys.ens.fr

¹ Fermionic DM absorption models [4–6] allow XENON1T and SUPER-K to probe masses down to $\sim \mathcal{O}(10 \text{ keV})$ and $\sim \mathcal{O}(1 \text{ MeV})$ respectively

II. BLAZAR JET SPECTRUM

Blazars are characterized by a non-thermal spectral energy distribution (SED). This spectrum has a low energy peak in the infra-red or X-ray region, which has been accepted to be due to synchrotron emission of electrons in the jet [30]. Another peak at γ -ray frequencies could be due to highly relativistic protons [31–35], as motivated by the recent IceCube detection [36–38] of a high energy neutrino from TXS 0506+056 blazar. Since DM considered in this work is electrophilic, at tree level it can only interact with electrons. Therefore, we are only concerned with the blazar jets' electron spectrum.

We follow the procedure laid out in Ref. [27, 28] to compute the spectrum of the energetic electrons in the blazar jets, assuming ‘‘Blob geometry’’ model [39]. In this model, the energetic particles in the blazar jets move isotropically in a ‘‘blob’’ frame, as the blob traverses outwards along the jet axis. The Lorentz boost factor of the blob is given by $\Gamma_B = (1 - \beta_B^2)^{-1/2}$, where β_B is the blob's propagation speed. The inclination of the jet axis with respect to the line of sight (LOS) is taken to be θ_{LOS} .

In the blob frame, the energetic electrons follow a power law distribution with a high and a low energy cutoff ($\gamma'_{\text{max},e}$ and $\gamma'_{\text{min},e}$ respectively). This spectrum can then be frame transformed to the observer's rest frame (for details of the derivation, see [27]), given by :

$$\frac{d\Gamma_e}{dT_e d\Omega} = \frac{c_e}{4\pi} \Gamma_B^{-\alpha_e} \left(1 + \frac{T_e}{m_e}\right)^{-\alpha_e} \times \frac{\beta_e (1 - \beta_e \beta_B \mu)^{-\alpha_e}}{\sqrt{(1 - \beta_e \beta_B \mu)^2 - (1 - \beta_e^2)(1 - \beta_B^2)}} \quad (1)$$

$$c_e = \frac{L_e}{m_e^2 \Gamma_B^2} \times \begin{cases} (2 - \alpha_e) / [(\gamma'_{\text{max},e})^{2-\alpha_e} - (\gamma'_{\text{min},e})^{2-\alpha_e}] & \text{if } \alpha_e \neq 2 ; \\ 1 / \log(\gamma'_{\text{max},e} / \gamma'_{\text{min},e}) & \text{if } \alpha_e = 2. \end{cases} \quad (5)$$

The parameters $\gamma'_{\text{min},e}$, $\gamma'_{\text{max},e}$, α_e , L_e and \mathcal{D} are fitted to the SED of a blazar. The doppler factor is assumed to be either $2\Gamma_B$ or Γ_B . These two cases correspond to TXS 0506+056 ($\theta_{\text{LOS}} = 0$) and BL Lacertae ($\theta_{\text{LOS}} \sim 3.8^\circ$). All the parameters required to find the blazar jet spectrum of TXS 0506+056 and BL Lacertae, along with the blazar redshift and luminosity distance (d_L) are mentioned in Table I. The electron spectrum is plotted in Fig. 1.

III. DM DENSITY PROFILE

N-body simulations and observations are not sensitive at subparsec sizes, thus the DM distribution near Galac-

tic center is not well known. The central supermassive black hole (SMBH) can have a considerable impact on DM density if the SMBH grows adiabatically, i.e., on a timescale much longer than its dynamical timescale. The DM density in a region corresponding to the sphere of gravitational influence of the black hole (BH) is expected to be significantly enhanced [42]. This results in a morphological feature known as a DM spike, which corresponds to a DM profile with a power law scaling $\rho(r) \propto r^{-\gamma_{\text{sp}}}$ [42]. Here $\gamma_{\text{sp}} = \frac{9-2\gamma}{4-\gamma}$ commonly ranges from 2.25 to 2.5, depending on the slope of the initial DM halo distribution, γ . In this work, we assume the initial central DM profile is Navarro-Frenk-White, $\gamma = 1$. Also, for DM annihilating with cross-section $\langle\sigma v\rangle_{\text{ann.}}$, the innermost region of the DM spike is de-

$$\mu(\bar{\mu}_s, \phi_s) = \bar{\mu}_s \cos \theta_{\text{LOS}} + \sin \phi_s \sin \theta_{\text{LOS}} \sqrt{1 - \bar{\mu}_s^2} \quad (2)$$

where ϕ_s is the azimuth with respect to the LOS. $\bar{\mu}_s$ is related to the kinetic energy of the blazar jet electron and the kinetic energy (T_χ) transferred to the DM, as follows :

$$\bar{\mu}_s(T_e, T_\chi) = \left[1 + \frac{T_\chi^{\text{max}} - T_\chi}{T_\chi} \frac{(m_e + m_\chi)^2 + 2m_\chi T_e}{(T_e + m_e + m_\chi)^2}\right]^{-1/2} \quad (3)$$

Now, c_e is a normalisation constant which is determined from the blazar jet electron luminosity (L_e), where the latter depends on c_e as [27, 40] :

$$L_e = c_e m_e^2 \Gamma_B^2 \int_{\gamma'_{\text{min},e}}^{\gamma'_{\text{max},e}} (\gamma'_e)^{1-\alpha_e} d\gamma'_e, \quad (4)$$

and thus c_e is simply given by :

tic center is not well known. The central supermassive black hole (SMBH) can have a considerable impact on DM density if the SMBH grows adiabatically, i.e., on a timescale much longer than its dynamical timescale. The DM density in a region corresponding to the sphere of gravitational influence of the black hole (BH) is expected to be significantly enhanced [42]. This results in a morphological feature known as a DM spike, which corresponds to a DM profile with a power law scaling $\rho(r) \propto r^{-\gamma_{\text{sp}}}$ [42]. Here $\gamma_{\text{sp}} = \frac{9-2\gamma}{4-\gamma}$ commonly ranges from 2.25 to 2.5, depending on the slope of the initial DM halo distribution, γ . In this work, we assume the initial central DM profile is Navarro-Frenk-White, $\gamma = 1$. Also, for DM annihilating with cross-section $\langle\sigma v\rangle_{\text{ann.}}$, the innermost region of the DM spike is de-

Parameter	TXS 0506+056	BL Lacertae
Redshift	0.337	0.069
d_L	1835.4 Mpc	322.7 Mpc
M_{BH}	$3.09 \times 10^8 M_\odot$	$8.65 \times 10^7 M_\odot$
Γ_B	20	15
θ_{LOS}	0°	3.82°
α_e	2	3.5
$(\gamma'_{\text{min},e}, \gamma'_{\text{max},e})$	$(500, 1.3 \times 10^4)$	$(700, 1.5 \times 10^4)$
L_e (erg/s)	1.32×10^{44}	8.7×10^{42}

TABLE I: Model parameters for TXS 0506+056 [32] and BL Lacertae blazars [41].

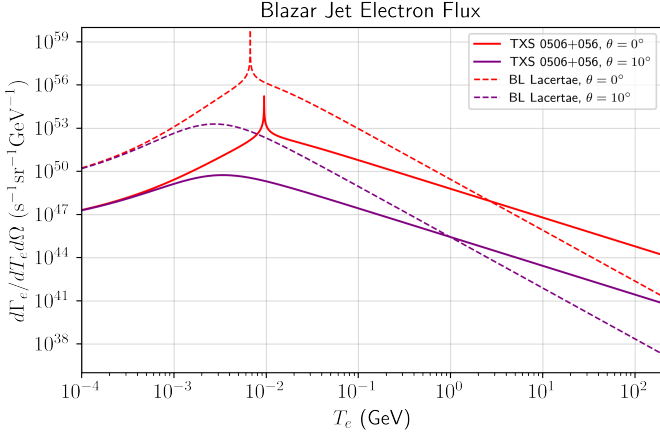


FIG. 1: The electron spectrum in the observer’s frame is plotted above, for the blazars TXS 0506+056 (solid lines) and BL Lacertae (dashed lines). The spectrum is shown for two different polar angles : $\theta = 0^\circ$ (in red), $\theta = 10^\circ$ (purple). For larger kinetic energies ($T_e \gtrsim 10$ GeV), the electron flux from TXS 0506+056 blazar exceeds the flux from BL Lacertae.

pleted because DM particles annihilate efficiently on account of high DM density, leading to an “annihilation plateau” density given by

$$\rho_{\text{sat}} = \frac{m_\chi}{\langle \sigma v \rangle_{\text{ann}} t_{\text{BH}}}, \quad (6)$$

where $t_{\text{BH}} \sim 10^9$ yrs [28] is the age of the BH. The DM density profile in such a spike is given by

$$\rho(r) = \begin{cases} 0 & r < 4R_S \\ \rho_{\text{sat}} & 4R_S \leq r < R_{\text{sat}} \\ \mathcal{N}_1 r^{-\gamma_{\text{sp}}} & R_{\text{sat}} \leq r < R_{\text{sp}} \\ \mathcal{N}_2 r^{-\gamma} & r \geq R_{\text{sp}} \end{cases}, \quad (7)$$

where $R_S = 2GM/c^2$ is the Schwarzschild radius of the BH, $R_{\text{sp}} = 10^5 R_S$ is the radius of the spike [40] and $\rho(r)$ goes to zero in the region $r < 4R_S$ due to DM particles being captured by the SMBH. The saturation density ρ_{sat} and the saturation radius R_{sat} are related by the equality $\rho(R_{\text{sat}}) = \rho_{\text{sat}}$. In this work, the normalization \mathcal{N}_1 of ρ is determined by observing that the

mass of the spike is of the same order as M_{BH} within the spike radius [43] and \mathcal{N}_2 is determined by observing the continuity of the profile at R_{sp} . However, this choice of normalisation (\mathcal{N}_1) is only an optimistic upper limit, and there could be way less DM close to the BH. We show, in Appendix :A, how the main results of our work (i.e. the exclusion limits in Figs. 5,6) scale for the choice of different normalisations \mathcal{N}_1 .

For a pre-existent DM halo with $\gamma = 1$, the final DM profile near BH corresponds to $\gamma_{\text{sp}} = 7/3$. A more realistic model was obtained in Ref. [44], where the time-evolution of dark matter distribution was investigated on sub-parsec scales. This implied softening of the DM density spike, due to scattering of DM by stars and capture of DM particles by the SMBH, dampening it to $\gamma_{\text{sp}} = 3/2$. Thus, in this work, we consider both the DM profile parameters $\gamma_{\text{sp}} = 7/3$ and $\gamma_{\text{sp}} = 3/2$ along with two extreme values of $\langle \sigma v \rangle_{\text{ann}}$. We define these as

$$\text{Profile 1: } \rho(R_{\text{sat}} \leq r < R_{\text{sp}}) = \mathcal{N}_1 r^{-7/3}$$

$$\text{Profile 2: } \rho(R_{\text{sat}} \leq r < R_{\text{sp}}) = \mathcal{N}_1 r^{-3/2}.$$

It should be noted that the formation of DM spike can be influenced by various factors, including mergers with other galaxies and the distance between the BH and the Galactic center [43, 44]. While some of these uncertainties have been addressed in studies of the formation of the DM spike in the Milky Way, no such studies exist for the galaxy considered in our paper. Therefore, we provide a preliminary analysis of the potential effects of DM close to a BH in a galactic center.

For each of these profiles, the two benchmark points (BMPs) are defined as:

BMP 1: No DM annihilation, i.e., $\langle \sigma v \rangle_{\text{ann}}|_{\text{tot}} = 0$. Here, we assume that the DM annihilation is forbidden by some symmetry.

BMP 2: $\langle \sigma v \rangle_{\text{ann}}|_{\text{tot}} = 3 \times 10^{-26} \text{ cm}^3 \text{ s}^{-1}$, thermal relic cross-section.

Another quantity relevant to the computation of the BBDM flux is the line of sight (LOS) integral of DM density around the blazar. This provides a measure of the number of DM particles being boosted by the blazar. At a certain distance r from the blazar, it is defined as

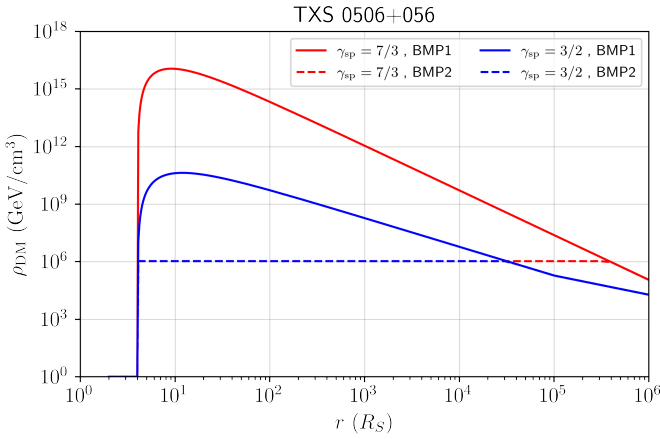
$$\Sigma_{\text{LOS}}(r) = \int_{r_{\text{min}}}^r \rho(r') dr' \quad (8)$$

where r_{min} is the distance from the SMBH from where the blazar jet starts. To get a measure of all boosted DM particles, we want the LOS integral at large distances ($r \gg 10^5 R_S$), and we define $\Sigma_{\text{LOS}}^{\text{tot}} = \Sigma_{\text{LOS}}(r \gg 10^5 R_S)$.

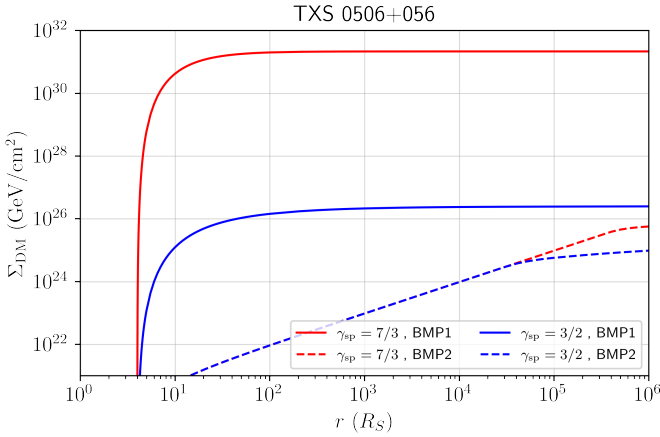
In this work, we will study BBDM flux from TXS 0506+056 and BL Lacertae, and for these blazars, r_{min} lies within $100R_S$ [32, 40, 41]. We take $r_{\text{min}} = 4R_S$, noting that $\Sigma_{\text{LOS}}^{\text{tot}}$ is independent of choice of r_{min} for models which allow for DM pair annihilation. For no

DM annihilation, $\Sigma_{\text{LOS}}^{\text{tot}}$ decreases by an order of magnitude when r_{min} is changed to $100R_S$.

The DM density and L.O.S. integral profiles are plotted in Fig 2 for two benchmark points. For both DM density profiles, BMP1 yields a larger spike and a larger LOS integral ($\Sigma_{\text{LOS}}^{\text{tot}}$). This results in a larger BBDM flux and consequently a stronger exclusion bound on DM-electron interaction cross section. Hence, one can expect models with no DM annihilation to yield better bounds. Moreover, even though the LOS integral for the idealistic spike (Profile 1) is very large and thus results in substantial BBDM flux, the more realistic profile (Profile 2) with a softer spike would lead to a much smaller LOS integral, and hence a much weaker exclusion bound.



(a) DM Density Profile



(b) LOS integral profile

FIG. 2: The profiles of ρ_{DM} (Fig. 2a) and Σ_{DM} (Fig. 2b) are plotted above for TXS 0506+056 blazar parameters. The DM mass chosen for these figures is $m_\chi = 1$ MeV. Profile 1 (red) and Profile 2 (blue) are plotted for BMP 1 (solid curve) and BMP 2 (dashed curve). BL Lacertae, on the other hand, is less massive than TXS 0506+056, and yields a larger spike (for BMP1) at a smaller distance from the BH (See text for more details).

IV. BLAZAR BOOSTED DARK MATTER FLUX AND EVENT RATE

DM particles are boosted via elastic collisions with the relativistic electrons in the blazar jet. The DM differential flux resulting out of collision with the electrons is obtained as follows :

$$\frac{d\phi_\chi}{dT_\chi} = \frac{\Sigma_{\text{DM}}^{\text{tot}}}{2\pi m_\chi d_L^2} \int_0^{2\pi} d\phi_s \int_{T_e^{\text{min}}(T_\chi, \phi_s)}^{T_e^{\text{max}}(T_\chi, \phi_s)} dT_e \times \frac{d\sigma_{\chi e}}{dT_\chi} \frac{d\Gamma_e}{dT_e d\Omega}, \quad (9)$$

where $\sigma_{\chi e}$ is the DM-electron interaction cross section. The integration over ϕ_s becomes trivial in case of TXS 0506+056, where the system is symmetric about LOS, and we can simply set $\mu = \bar{\mu}_s$ (from Eqn. (2)).

The maximal kinetic energy of the blazar jet electrons along LOS is given by $T_{e,\text{jet}}^{\text{max}} = m_e (\gamma'_{\text{max},e} \Gamma_B^{-1} (1 - \beta_B \cos \theta_{\text{LOS}})^{-1} - 1)$. This is set as the upper bound of the integral on T_e in Eqn. (9). The lower bound is set by the minimum kinetic energy required for scattering, given by

$$T_e^{\text{min}} = \left(\frac{T_\chi}{2} - m_e \right) \left[1 \pm \sqrt{1 + \frac{2T_\chi(m_e + m_\chi)^2}{m_\chi(T_\chi - 2m_e)^2}} \right] \quad (10)$$

with + and - applicable for $T_\chi > 2m_e$ and $T_\chi < 2m_e$ respectively. However, the kinetic energy of the slowest electrons in the blazar jets could be larger than T_e^{min} . In such a case, the kinetic energy of the least energetic electron in the jet, given by $T_{e,\text{jet}}^{\text{min}} = m_e (\gamma'_{\text{min},e} \Gamma_B^{-1} (1 - \beta_B \cos \theta_{\text{LOS}})^{-1} - 1)$, sets the lower bound of the integral in Eqn. (9).

The differential cross section ($d\sigma_{\chi e}/dT_\chi$) of the DM-blazar jet electron interaction is given by,

$$\frac{d\sigma_{\chi e}}{dT_\chi} = \frac{|\mathcal{M}|^2}{16\pi s_e} \frac{1}{T_\chi^{\text{max}}} \quad (11)$$

where \mathcal{M} is the interaction matrix element, a function of T_χ and T_e . s_e is the centre of momentum energy for the electron-DM collision given by :

$$s_e = (m_\chi + m_e)^2 + 2m_\chi T_e, \quad (12)$$

and T_χ^{max} is the maximum kinetic energy that can be imparted to a DM particle by a blazar jet electron of energy T_e is given by :

$$T_\chi^{\text{max}} = \frac{T_e^2 + 2m_e T_e}{T_e + (m_e + m_\chi)^2 / (2m_\chi)} \quad (13)$$

TXS 0506+056 blazar is more massive as compared to BL Lacertae. Keeping this in mind allows us to qualitatively compare the DM density spikes and LOS integrals from these two blazars. For BMP1, the normalisation factor \mathcal{N}_1 of the density profile is proportional

to $M_{\text{BH}}^{1/3}$ for Profile 1, while for Profile 2, \mathcal{N}_1 is proportional to $M_{\text{BH}}^{-1/2}$. The LOS values for both profiles vary as M_{BH}^{-1} , hence BL Lac yields a larger spike as well as a larger LOS value for BMP1. However, for BMP2, most of the DM density profile is determined by ρ_{sat} , which is independent of M_{BH} . The LOS values of the two blazars are thus not significantly different for BMP2. TXS 0506+056 is also further away from us as compared to BL Lacertae. Overall, the contribution to the DM flux coming from the factors $(\Sigma_{\text{LOS}}/d_L^2)$ outside the integrals in Eqn. (9) is expected to be significantly larger for BL Lacertae than TXS 0506+056.

In spite of this, we note in Figs. 3 and 4 that the flux of DM particles boosted by TXS 0506+056 is larger than the BBDM flux of BL Lacertae, for more energetic DM particles ($T_\chi \gtrsim 10$ GeV). This is because, the kinetic energy range of the electron responsible for boosting the DM particle to energies greater than 10 GeV is roughly $T_e \gtrsim 10$ GeV. For this energy range, the electron spectrum in TXS blazar is larger than that of BL Lac (Fig. 1). As a result of this, we expect stronger bounds to arise from TXS blazar.

The obtained boosted DM flux will yield the following rate of electron recoil events in SUPER-K

$$\frac{dR}{dE_R} = \aleph \int_{T_\chi^{\min}}^{\infty} dT_\chi \frac{d\phi_\chi}{dT_\chi} \frac{d\sigma_{\chi e}}{dE_R} \quad (14)$$

where $\aleph = 7.5 \times 10^{33}$ is the effective number of target electrons in SUPER-K [3], and $d\sigma_{\chi e}/dE_R$ is the differential DM-target electron interaction cross section, given by

$$\frac{d\sigma_{\chi e}}{dE_R} = \frac{|\mathcal{M}|^2}{16\pi s_\chi} \frac{1}{E_R^{\max}} \quad (15)$$

where s_χ is centre of momentum energy for the DM-target electron collision which can be obtained from Eqn. (12) under the substitution : $m_\chi \leftrightarrow m_e$ and $T_e \rightarrow T_\chi$. E_R^{\max} is the maximum possible recoil in the detector, that can be imparted by a DM particle with kinetic energy T_χ , and can be obtained from Eqn. (13) with the appropriate substitutions mentioned before.

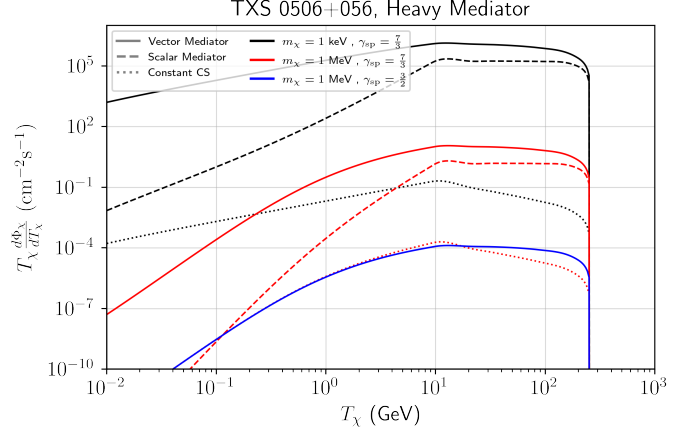
To get total number of expected recoil events ($N_{e\chi}$) in a certain energy bin, Eqn. (14) needs to be integrated over E_R , as follows

$$N_{e\chi} = \aleph T_{\text{exp}} \int_{E_{R,\min}}^{E_{R,\max}} dE_R \int_{T_\chi^{\min}}^{\infty} dT_\chi \frac{d\phi_\chi}{dT_\chi} \frac{d\sigma_{\chi e}}{dE_R} \quad (16)$$

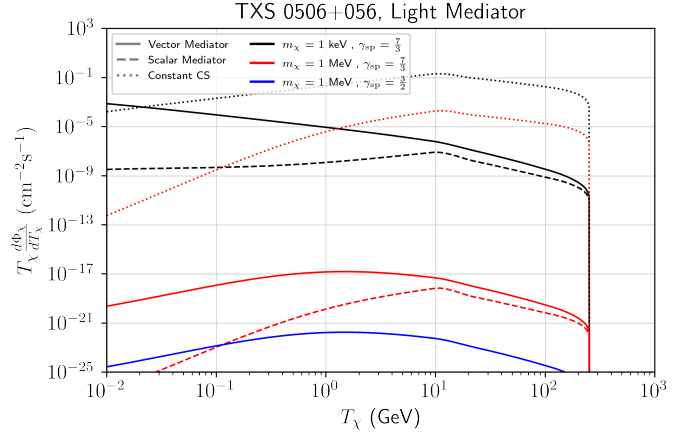
where $T_{\text{exp}} = 2628.1$ days is the exposure time [3], and $[E_{R,\min}, E_{R,\max}]$ is the recoil energy range of each bin.

V. SIMPLIFIED DM MODEL

We assume that a fermionic DM particle χ , of mass m_χ , only interacts with electrons. This scenario is possible in several leptophilic particle DM models [45–54].



(a) BBDM flux for heavy mediator scenario



(b) BBDM flux for light mediator scenario

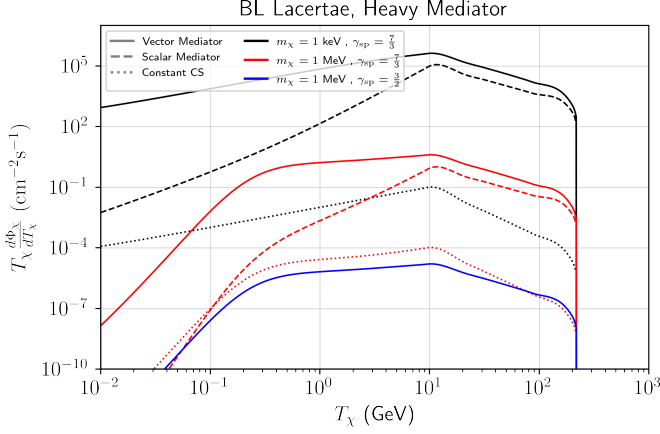
FIG. 3: Flux of DM particles, boosted by energetic electrons in the jets of TXS 0506+056 blazar, is plotted above, for heavy (3a) and light (3b) mediators. The parameters chosen for the above plots are $\bar{\sigma}_{e\chi} = 10^{-30} \text{ cm}^2$ and BMP1. The vector and the scalar mediator cases have been plotted in solid and dashed lines respectively. For comparison, DM flux for constant cross section scenario have also been plotted in dotted lines. Two DM masses have been considered, $m_\chi = 1 \text{ keV}$ (plotted in black) and $m_\chi = 1 \text{ MeV}$ (plotted in red) for DM density Profile 1 (i.e. $\gamma_{\text{sp}} = 7/3$). To avoid overcrowding, only vector mediator case is considered for Profile 2 (i.e. $\gamma_{\text{sp}} = 3/2$), and BBDM flux is plotted (in blue) corresponding to DM mass $m_\chi = 1 \text{ MeV}$. Clearly, Profile 2 yields a smaller BBDM flux as compared to Profile 1.

Additionally, the electron-DM interaction is mediated by a scalar or vector particle, given as

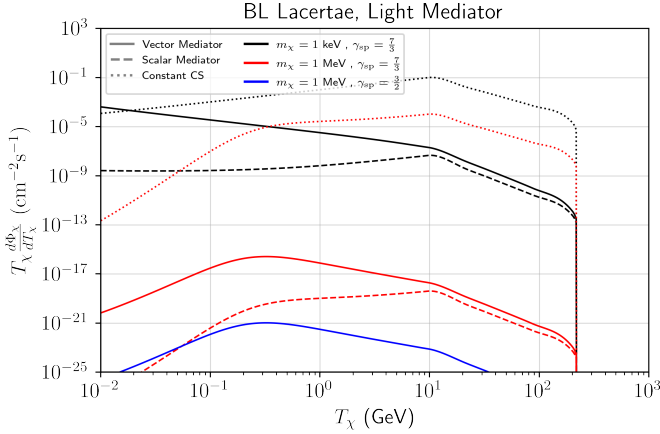
$$\mathcal{L} = g_\chi \phi \bar{\chi} \chi + g_e \phi \bar{e} e \quad \text{or} \quad (17)$$

$$= g_{\chi A'} A'_\mu \bar{\chi} \gamma^\mu \chi + g_{e A'} A'_\mu \bar{e} \gamma^\mu e \quad (18)$$

For simplicity, we will drop A' and ϕ from subscripts in the coupling constants such that g_χ (g_e) is the coupling constant of the dark mediator to the DM particle (electron). Next, we provide the differential cross-section for



(a) BBDM flux for heavy mediator scenario



(b) BBDM flux for light mediator scenario

FIG. 4: Flux of DM particles, boosted by energetic electrons in the jets of BL Lacertae blazar, is plotted above, for heavy (4a) and light (4b) mediators. The parameters chosen for the above plots are $\bar{\sigma}_{e\chi} = 10^{-30} \text{ cm}^2$ and BMP1. The vector and the scalar mediator cases have been plotted in solid and dashed lines respectively. For comparison, DM flux for constant cross section scenario have also been plotted in dotted lines. Two DM masses have been considered, $m_\chi = 1 \text{ keV}$ (plotted in black) and $m_\chi = 1 \text{ MeV}$ (plotted in red) for DM density Profile 1 (i.e. $\gamma_{sp} = 7/3$).

To avoid overcrowding, only vector mediator case is considered for Profile 2 (i.e. $\gamma_{sp} = 3/2$), and BBDM flux is plotted (in blue) corresponding to DM mass $m_\chi = 1 \text{ MeV}$. Clearly, Profile 2 yields a smaller BBDM flux as compared to Profile 1.

different operators and inspect the effect of the Lorentz structure. For that, we define the following quantities :

$$\mathbb{M}^2 = \frac{16g_e^2 g_\chi^2 m_e^2 m_\chi^2}{(q_{\text{ref}}^2 - m_i^2)^2} \quad (19)$$

$$\bar{\sigma}_{e\chi} = \frac{\mu_{e\chi}^2}{16\pi m_e^2 m_\chi^2} \mathbb{M}^2 \quad (20)$$

where $q_{\text{ref}} = \alpha m_e$ is the reference momentum transferred. Here m_i is the mass of the dark mediator ($i = A', \phi$ for vector, scalar mediator) and $\mu_{e\chi}$ is the reduced mass of the DM-electron system. We also define a form factor,

$$F_{\text{DM}}^2(q^2) = |\mathcal{M}|^2 / \mathbb{M}^2 \quad (21)$$

This factor contains the energy dependence arising in the differential cross section $d\sigma_{\chi e} / dT_\chi$ due to the blazar jet electrons boosting the DM particles and the Lorentz structure of the interaction. The explicit form of F_{DM} depends on the model of DM and mediator considered.

A similar form factor, F_{rec} , contains the energy dependence in the differential cross section $d\sigma_{\chi e} / dE_R$ arising due to the interaction of relativistic DM particles with the electrons in SUPER-K, and can be obtained from the form factor F_{DM} of Eqn. (21) by making the substitutions : $m_e \leftrightarrow m_\chi$, $T_\chi \rightarrow E_R$ and $T_e \rightarrow T_\chi$.

Hence the differential cross sections, $d\sigma_{\chi e} / dT_\chi$ and $d\sigma_{\chi e} / dE_R$, relevant in the DM-blazar jet electron scattering and DM scattering at the detector end respectively, are given by :

$$\frac{d\sigma_{\chi e}}{dT_\chi} = \bar{\sigma}_{e\chi} \frac{m_e^2 m_\chi^2}{\mu_{e\chi}^2} \frac{F_{\text{DM}}^2(q^2)}{s_{\text{CR}} T_\chi^{\text{max}}} \quad (22)$$

and,

$$\frac{d\sigma_{\chi e}}{dE_R} = \bar{\sigma}_{e\chi} \frac{m_e^2 m_\chi^2}{\mu_{e\chi}^2} \frac{F_{\text{rec}}^2(q^2)}{s_\chi E_R^{\text{max}}} \quad (23)$$

Under the energy independent approximation for the cross section, the differential cross section would simply be :

$$\frac{d\sigma_{\chi e}}{dT_\chi} = \frac{\bar{\sigma}_{e\chi}}{T_\chi^{\text{max}}}, \quad \frac{d\sigma_{\chi e}}{dE_R} = \frac{\bar{\sigma}_{e\chi}}{E_R^{\text{max}}} \quad (24)$$

A. Scalar Mediator

Considering a scalar mediator (denoted as ϕ), one can calculate F_{DM}^2 for the interaction between electrons in blazar jets and non-relativistic DM, using Eqn. (21) to obtain

$$F_{\text{DM}}^2(q) = \frac{(q_{\text{ref}}^2 - m_\phi^2)^2}{(q^2 - m_\phi^2)^2} \frac{(2m_\chi + T_\chi)(2m_e^2 + m_\chi T_\chi)}{4m_\chi m_e^2} \quad (25)$$

The differential cross section ($d\sigma_{\chi e} / dT_\chi$) w.r.t. the DM energy (T_χ), is :

$$\frac{d\sigma_{\chi e}}{dT_\chi} = \bar{\sigma}_{e\chi} \frac{(q_{\text{ref}}^2 - m_\phi^2)^2}{(q^2 - m_\phi^2)^2} \left\{ \frac{m_\chi}{4\mu_{e\chi}^2} \frac{(2m_\chi + T_\chi)(2m_e^2 + m_\chi T_\chi)}{s_{\text{CR}} T_\chi^{\text{max}}} \right\} \quad (26)$$

The form factor F_{rec} and the differential cross-section w.r.t. the recoil energy of the detector ($d\sigma_{\chi e}/dE_R$) are obtained from Eqn. (25) and Eqn. (26) by performing the substitutions prescribed in the previous section, viz. $m_e \leftrightarrow m_\chi$, $T_\chi \rightarrow E_R$, $T_e \rightarrow T_\chi$, $s_e \rightarrow s_\chi$.

B. Vector Mediator

Using a similar treatment for the vector mediator (denoted by A'), we find that

$$F_{\text{DM}}^2(q^2) = \frac{(q_{\text{ref}}^2 - m_{A'}^2)^2}{(q^2 - m_{A'}^2)^2} \frac{1}{2m_\chi m_e^2} \left(2m_\chi (m_e + T_e)^2 - T_\chi \left\{ (m_e + m_\chi)^2 + 2m_\chi T_e \right\} + m_\chi T_\chi^2 \right) \quad (27)$$

and,

$$\frac{d\sigma_{\chi e}}{dT_\chi} = \bar{\sigma}_{e\chi} \frac{(q_{\text{ref}}^2 - m_{A'}^2)^2}{(q^2 - m_{A'}^2)^2} \frac{m_\chi}{2\mu_{e\chi}^2 s_{\text{CR}} T_\chi^{\text{max}}} \left\{ 2m_\chi (m_e + T_e)^2 - T_\chi \left\{ (m_e + m_\chi)^2 + 2m_\chi T_e \right\} + m_\chi T_\chi^2 \right\} \quad (28)$$

VI. RESULTS

The effect of including energy dependence in DM-electron interaction can be seen from the BBDM flux plots, given in Figs. 3 and 4. Profile 1 of DM density clearly gives larger BBDM flux as compared to Profile 2, as expected from larger DM spike for profile 1 shown in Fig. 2 in Section III. For DM to register event at SUPER-K, kinetic energies greater than ~ 0.1 GeV are relevant. In this energy range, the heavy mediator scenario gives much larger BBDM flux as compared to the constant cross section case, while on the other hand, the light mediator regime yields a much smaller BBDM flux. From this, we expect the exclusion limit on DM-electron interaction, arising from light mediator regime, to be extremely weak. Since the vector mediator case gives slightly larger BBDM flux as compared to the scalar mediator scenario, we hope for moderately better bounds from vector mediators. Also, since for any given DM Profile or BMP, the BBDM flux is larger for smaller mass DM particles, we can expect bounds to grow stronger for lighter DM particle. Finally, the BBDM flux plots terminate at a certain value of T_χ because the blazar jet electrons boosting the DM particles have an upper cutoff on their energies (for TXS 0506+056 jets, $T_{e,\text{jet}}^{\text{max}} \sim 260$ GeV and for BL Lacertae jets, $T_{e,\text{jet}}^{\text{max}} \sim 225$ GeV).

Taking into account the signal efficiency of each recoil bin (ϵ_{sig}), the exclusion limit on $\bar{\sigma}_{e\chi}$ is obtained by

$$N_{e\chi} \epsilon_{\text{sig}} < N_{\text{B}}, \quad (29)$$

where $N_{e\chi}$, obtained from Eqn. (16), is the number of expected recoil events arising out of collision of target

electron with DM particles boosted by the blazars. N_{B} ($B = \text{TXS, BL}$ for TXS 0506+056 and BL Lacertae) are the 95% CL upper limits on number of events from the blazars.

Three energy bins were considered in the analysis released by SUPER-K collaboration [3]. The total number of events, the Monte Carlo simulation of the background, signal efficiency and spatial distribution of events were provided for each bin. One can use this data to select signals from a certain ‘‘searching cone’’ in the direction of the blazar. This removes the majority of the background from the data, increasing sensitivity. The selected signal is then used in the standard Poisson method [55] to yield 95% CL upper limit on expected number of events (N_{B}) for each of the three bins. This analysis was performed by the authors of Ref. [28], and we use their results (i.e. N_{B}), summarised in Table II. (For details of the analysis, see [3, 9, 10, 28]). This gives us all the numbers relevant to finding exclusion limits on $\bar{\sigma}_{e\chi}$ using Eqn. (29).

Bins	$E_R(\text{GeV})$	ϵ_{sig}	N_{TXS}	N_{BL}
Bin 1	(0.1, 1.33)	93.0%	19.39	17.27
Bin 2	(1.33, 20)	91.3%	3.42	6.27
Bin 3	(20, 10^3)	81.1%	2.98	2.98

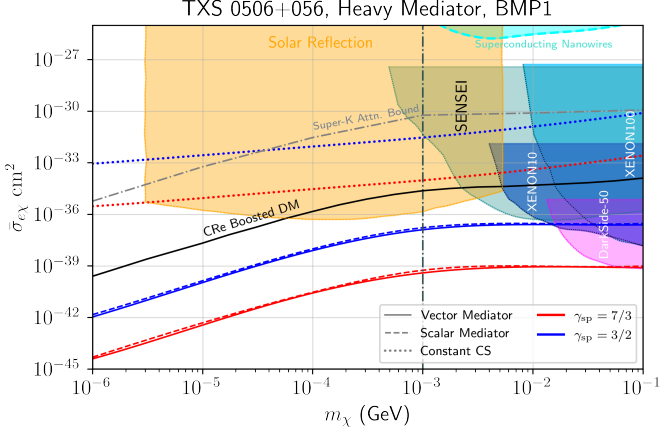
TABLE II: Signal efficiency (ϵ_{sig}) and 95% CL upper limits on number of events (N_{TXS} and N_{BL}) from the blazars, provided for the three recoil bins of SUPER-K.

SUPER-K is located deep underground to reduce background. As a result, the DM flux entering the detector is significantly attenuated, primarily as a result of its interaction with electrons on the Earth’s surface, and this gives rise to the attenuation bound in the exclusion plot. We provide an approximation of the attenuation bound, which is the cross section for which the DM particle with $T_\chi \sim 10$ GeV can impart the threshold recoil energy in the detector. For this, we solve the following equation to calculate the energy (T_r) lost by the DM

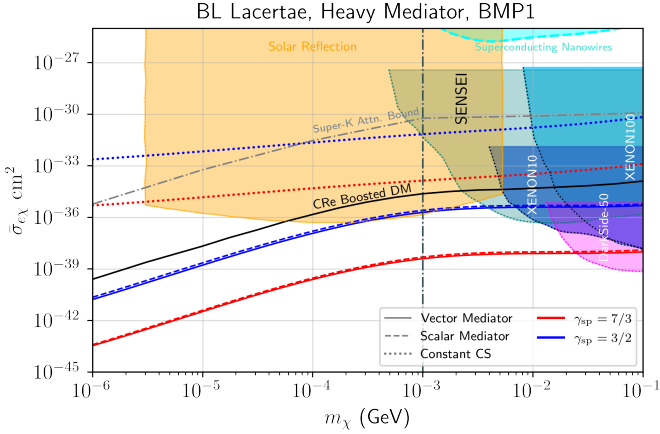
$$\frac{dT_\chi}{dx} = - \sum_T n_T \int_0^{T_r^{\text{max}}} \frac{d\sigma}{dT_r} T_r dT_r \quad (30)$$

and estimate $\bar{\sigma}_{e\chi}$ so that kinetic energy of the DM particle at depth z , denoted by T_χ^z , is the detector threshold E_{th} (we consider $E_{\text{th}} = 100$ MeV corresponding to Bin 1), for an initial kinetic energy $T_{\chi,\text{in}} \sim 10$ GeV. The area bounded by the attenuation bound and the exclusion bound is ruled out by our analysis. In this work, we limit ourselves to elastic scattering and ignore backscattering of light DM particles into the atmosphere. Note that the attenuation limits exist only for the heavy mediators and this may also vary once a more elaborate study is performed, which we leave for future work.

The exclusion bound arising from SUPER-K data is shown in Figs. 5 and 6 in the heavy mediator regime for scalar and vector operators. Taking energy dependence into account, the exclusion bound is significantly



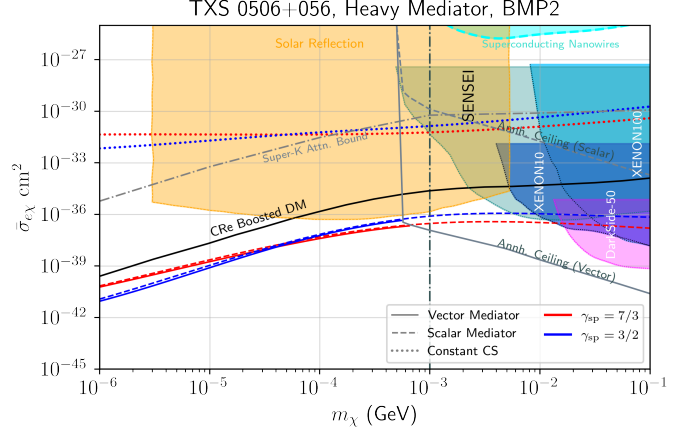
(a) Exclusion Bound for TXS 0506+056



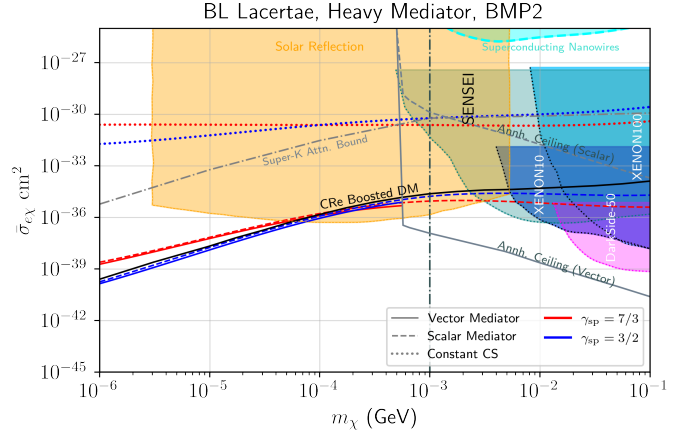
(b) Exclusion Bound for BL Lacertae

FIG. 5: The exclusion bound is plotted for the blazars TXS 0506+056 (5a) and BL Lacertae (5b), corresponding to BMP1. The cases considered are heavy vector mediator (plotted in solid lines), heavy scalar mediator (plotted in dashed lines) and constant cross section case (plotted in dotted lines). The various DM density profiles considered are Profile 1 (in red) and Profile 2 (in blue). The direct detection bounds from XENON10, XENON100, SENSEI [56–58] and DARKSIDE-50 [59] are also plotted. The BBN limits are shown by dotted-dashed curve. The bound arising due to DM attenuation is also given for heavy mediator scenario (plotted in grey). The area bounded by the attenuation bound and the exclusion bound is ruled out by our analysis. Exclusion limit from Superconducting Nanowires is provided in cyan color. Constraint due to solar reflection of DM [20, 60] is shown in amber color. The exclusion bound given by Cosmic Ray electron (CR) boosted DM [61] is plotted in black (See text for more details).

different compared to the bound obtained from constant cross section assumption. BMP1 sets a stronger bound as compared to BMP2, and DM density Profile 1 yields a better bound as compared to Profile 2. This is in agreement with what we expected from the density pro-



(a) Exclusion Bound for TXS 0506+056



(b) Exclusion Bound for BL Lacertae

FIG. 6: The exclusion bound is plotted for the blazars TXS 0506+056 (6a) and BL Lacertae (6b), corresponding to BMP2. The cases considered are heavy vector mediator (plotted in solid lines), heavy scalar mediator (plotted in dashed lines) and constant cross section case (plotted in dotted lines). The various DM density profiles considered are Profile 1 (in red) and Profile 2 (in blue). The direct detection bounds from XENON10, XENON100, SENSEI [56–58] and DARKSIDE-50 [59] are also plotted. The bound arising due to DM attenuation is also given for heavy mediator scenario (plotted in grey). The area bounded by the attenuation bound and the exclusion bound is ruled out by our analysis. The BBN limits are shown by dotted-dashed curve. Exclusion limit from Superconducting Nanowires is provided in cyan color. Constraint due to solar reflection of DM [20, 60] is shown in amber color. The exclusion bound given by Cosmic Ray electron (CR) boosted DM [61] is plotted in black (See text for more details).

files (Fig. 2) in Section III and the BBDM flux plots (Figs. 3a and 4a) in Section IV.

Amongst the three recoil bins in SUPER-K, the strongest bound is set by Bin 3 (Bin 2) for heavy mediator (constant cross section) cases. This result

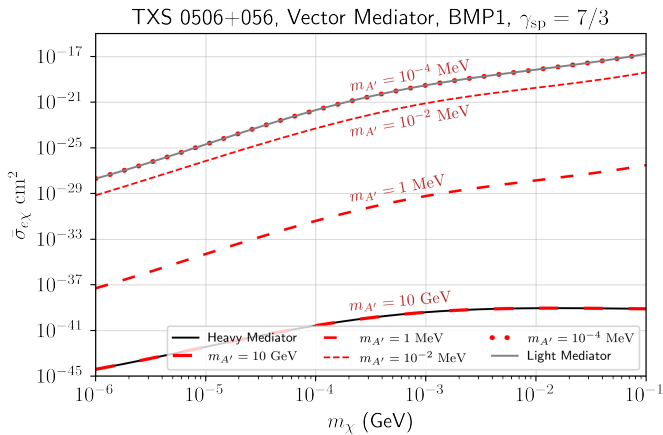


FIG. 7: The exclusion bound is plotted for the blazar TXS 0506+056 for various mediator masses, corresponding to the vector mediator scenario. The mediator masses chosen are 10 GeV, 1 MeV, 10^{-2} MeV and 10^{-4} MeV, all plotted in different linestyles. The bound for heavy (in black) and light (in grey) mediator regime is also plotted. The profiles chosen are DM density Profile 1, BMP1.

can be explained from the BBDM flux plots for TXS (Fig. 3a), by observing that the BBDM flux for heavy mediator is largest for $T_\chi \sim (20 \text{ GeV}, 10^3 \text{ GeV})$, which is nearly the DM energy range relevant to produce recoil in the third bin of SUPER-K. Similarly, for constant cross section case, the BBDM flux is largest for $T_\chi \sim (1 \text{ GeV}, 20 \text{ GeV})$, which is roughly the DM energy range relevant to the second recoil energy bin of SUPER-K. For BL Lacertae, even though the BBDM flux is largest $T_\chi \sim (1 \text{ GeV}, 20 \text{ GeV})$, which is the DM energy range relevant for Bin 2 (Fig. 4a), the event rate is largest for Bin 3 due to the larger size of the Bin. We also note that the constraints from TXS 0506+056 is stronger than constraints from BL Lacertae, which is what we expected from Fig. 1 and the discussion in Section IV.

In the exclusion bound plots (Figs. 5 and 6), we plot the most stringent limit on $\bar{\sigma}_{e\chi}$ coming from the three bins. Note that the bounds arising from scalar and vector mediators are almost same. The reason for this can be understood from Figs. 3 and 4, where we see that the BBDM flux for DM energies relevant to recoil Bin 3 of SUPER-K differs by $\sim \mathcal{O}(10)$ for the two operators, which results in very little difference in the exclusion limits. However, the limit coming from the three different bins can differ by ~ 2 or 3 orders of magnitude for certain m_χ , so a combined analysis of the three bins might change the bounds. We, however, leave out such an analysis from this work.

Since “heavy” and “light” mediator regimes are the convenient extremes of the actual DM model, the true exclusion bound would lie somewhere in between the bound set by these two regimes. Thus we compare the exclusion bound corresponding to various masses of the vector mediator for Profile 1 and BMP1 in Fig. 7. A

similar comparison and scaling exists for Profile 2 and BMP2. Clearly, a mediator of mass 10 GeV corresponds to the heavy regime, and a mediator of mass 10^{-4} MeV reproduces the exclusion limit set by the light mediator regime.

It should be noted that for $m_\chi \geq m_e$ the scattering cross-section and consequently the annihilation rate to e^-e^+ increases as we move to heavier DM particles in Fig. 6 (for $m_\chi \leq m_e$, $\sigma_{\text{ann}}^{e^-e^+} = 0$). The DM annihilation rate to e^-e^+ for scalar mediator is given by

$$\sigma_\phi = \frac{1}{16\pi} \frac{(g_e g_\chi)^2}{(q^2 - m_\phi^2)^2} \sqrt{\frac{s - 4m_e^2}{s - 4m_\chi^2}} \frac{(s - 4m_e^2)(s - 4m_\chi^2)}{s} \quad (31)$$

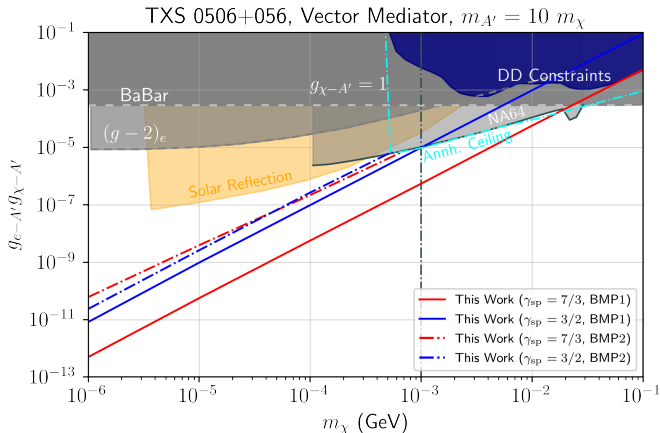
while for the vector mediator case, the annihilation rate is

$$\sigma_{A'} = \frac{1}{12\pi} \frac{(g_e g_\chi)^2}{(q^2 - m_{A'}^2)^2} \sqrt{\frac{s - 4m_e^2}{s - 4m_\chi^2}} \left[s + \frac{4m_\chi^2 m_e^2}{s} \right] \quad (32)$$

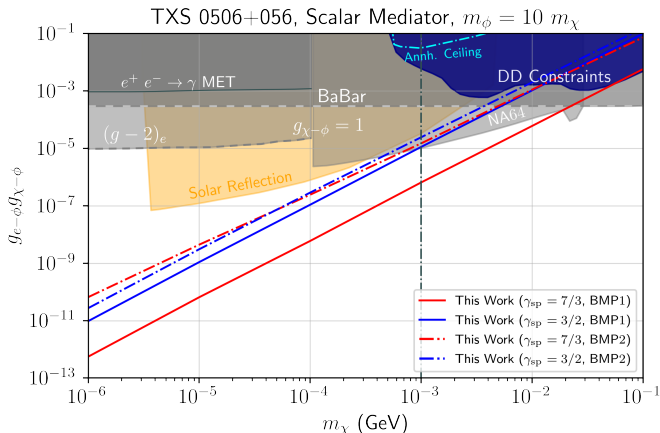
where s is centre of momentum frame energy and $v_\chi \approx 10^{-3}$ is DM velocity near centre of blazar. As a result, for large enough cross sections, DM annihilation rate can exceed $3 \times 10^{-26} \text{ cm}^3 \text{ s}^{-1}$, contradicting the rate assumed for BMP2. We refer to these cross sections as the annihilation ceiling and they are shown by gray curves in Fig. 6. For vector interaction, the annihilation ceiling established for a 100 GeV mediator is lower than the bound set by our work, thereby rendering the exclusion limits irrelevant. Hence, our exclusion limits for vector mediator are shown only for $m_\chi < m_e$. However, a significant parameter space remains constrained by our exclusion bounds for scalar interaction. There is no annihilation ceiling for BMP1 because it is presumed that annihilation is prohibited in BMP1 (for instance, in the case of asymmetric DM [62]).

Apart from blazars jets, Cosmic Ray electrons (CRE) provide yet another environment to produce boosted DM particles. Exclusion bound from CRE boosted DM, using SUPER-K data, is plotted along with our bounds in Figs. 5 and 6. Furthermore, Refs. [63, 64] propose a DM detection device with extremely low recoil trigger made using Superconducting Nanowires. The best bounds from such a prototype device is also shown. Currently our results are much stronger, but proposed devices with materials like NbN and Al might give better exclusions in the near future. Constraints from other direct detection experiments, such as XENON10, XENON100, SENSEI [56–58] and DARKSIDE-50 [59] are also shown. Exclusion limits from solar reflection of DM [20, 60] are important in the heavy mediator case, and are provided as well. Further, we translate our strongest bounds corresponding to blazar TXS 0506+056 onto the mass-coupling plane for $m_{A'(\phi)} = 10 m_\chi$, as shown in Fig. 8, along with other laboratory bounds from literature. Additionally, our benchmark allows for the constraint of g_e through the analysis of missing energy/momentum

signals observed in the dark photon search conducted by the NA64 collaboration [65] and the BABAR analysis [66]. It should be noted that when depicting these constraints for scalar mediators, we have taken a conservative approach, resulting in the elimination of a slightly larger portion of the parameter space than is strictly necessary.



(a) Constraints on couplings with Vector mediator.



(b) Constraints on couplings with Scalar mediator.

FIG. 8: The exclusion limit on $g_e g_\chi$ is plotted above for a) vector and b) scalar mediator for the blazar TXS 0506+056. The mediators are chosen to be 10 times more massive than the DM particles. Our bounds are plotted in red (Profile 1) and blue (Profile 2) curves, corresponding to BMP1 (solid lines) and BMP2 (dash-dotted lines). We also show bounds from BABAR [66], NA64 [65], Solar Reflection [20, 60], direct detection constraints [56–59], MET searches and $(g-2)_e$ constraints [67].

The cosmological constraints from Big Bang Nucleosynthesis (BBN) rule out thermal DM of $m_\chi \lesssim 10$ MeV stringently [67, 68]. However, these bounds can be relaxed in DM models down to 1 MeV with couplings by switching on couplings to neutrinos besides electrons [69]. Thus, BBN bounds are of significance when considering dark matter with a mass below 1 MeV ($m_\chi < 1\text{MeV}$). However, it is crucial to have a com-

prehensive understanding of the dark matter model in order to accurately evaluate these bounds. The CMB observations similarly constrain DM annihilating to an $e^- e^+$ pair severely [70]. An elaborate dark sector associated in these models can relax these constraints, so that DM mostly annihilate to other dark sector particles [71].

VII. SUMMARY & OUTLOOK

Blazars, in addition to being a key source of high energy electrons, are projected to have a DM density spike in their core due to DM accretion onto their SMBH. Despite large uncertainties from astrophysics and the unknown annihilation properties of dark matter in the density of the succeeding DM spike, strong bounds on the elastic scattering cross section for DM-electron scattering have been obtained in Ref. [28]. Here, we demonstrate how these limits change when the resulting energy dependence of the S-matrix for the associated vertex Lorentz structure is taken into consideration. We remain agnostic of the relic abundance mechanism since DM models might include an extended dark sector that has a significant impact on how much DM is there in the Universe right now. To that end, we derived limits using SUPER-K data. We found that the constraints on such energy-dependent scattering cross sections, which mostly depend on mediator mass, are at least several orders of magnitude tighter than the current limits from Blazars in the literature for the constant cross section assumption. Though the constant cross-section is a meaningful way to explain a concept, in reality it corresponds to a small parameter space of a DM model. Our bounds are, however, weakened if the mediator mass is sufficiently small. This is because the BBDM flux is orders of magnitude less than the constant cross-section in the relevant energy bin (see fig. 3b,4b). We also studied the less cuspy profile of the DM spike and realised that the constraints on $\bar{\sigma}_{e\chi}$ from BBDM are still significant compared to Cosmic ray boosted DM.

Another subtlety is that, in addition to relativistic electrons, blazars also contain energetic protons, which may contribute to the BBDM flux. However, the contribution is insignificant since the coupling with the proton is loop-suppressed if there is just a tree-level interaction of DM with charged electrons. Another natural assumption, inspired by the standard model's $SU(2)_L$ gauge symmetry, is that neutrino should have the same cross section with DM as charged leptons [72], allowing us to compare the current $\sigma_{e\chi} \sigma_{\nu\chi}$ limits for Cosmic ray boosted DM [19]. We intend to investigate this possibility in next work.

ACKNOWLEDGEMENTS

D.G. acknowledges support through the Ramanujan Fellowship and MATRICS Grant of the Department of Science and Technology, Government of India. D.S. has

received funding from the European Union’s Horizon 2020 research and innovation programme under grant agreement No 101002846, ERC CoG “CosmoChart”. The authors also thank Arka Banerjee and Susmita Ad-

hikari for valuable discussions. We thank Robert McGehee, Iason Baldes and Kalliopi Petraki for useful comments.

Appendix A: Scaling of exclusion limits with DM density spike

In this work, the normalization \mathcal{N}_1 in Eqn. (7) has been determined by observing that the mass of the spike is of the same order as M_{BH} within the spike radius. This, however, is only an optimistic limit and doesn’t have to hold. The DM density close to the BH could be practically far lesser, in which case the exclusion limits would be weaker. One can consider the following normalization for DM density profile

$$\int_{4R_S}^{R_{\text{sp}}} 4\pi r^2 \rho(r) dr = x M_{\text{BH}} \quad (\text{A1})$$

where $x \leq 1$ can be used to reduce number of DM particles in the spike. The DM density profiles and LOS integral for the two profiles $\gamma_{\text{sp}} = 7/3, 3/2$ and the two BMPs are given in Figs. 9 and 10, for three different values of x . The resultant exclusion limits are plotted for heavy vector mediator scenario in Fig. 11. Obviously, with decreasing number of DM particles in the spike, the exclusion limits become weaker. Clearly, the DM density and hence LOS integral profiles scale as $\sim x$ for BMP1, and hence the exclusion limits for various choices of normalisation scale as $\sim \frac{1}{\sqrt{x}}$ for both profiles. However, for BMP2, the proportionality is not that straightforward. The height (ρ_{sat}) of the DM density plateau at small r is independent of the choice of normalisation, but depends on m_χ . Depending on the mass of DM particle under consideration, there could be a significant number of DM particles left when x is reduced. For lighter DM particles, the DM density fall off behaviour with respect to x is different for Profile 1 and Profile 2, which is just a consequence of the parameterization of the density profile. As a result of this, for lighter DM and BMP2, the qualitative behaviour of the exclusion bounds, as x is reduced by orders of magnitude, is different in the two profiles.

-
- [1] E. Aprile *et al.* (XENON), Search for New Physics in Electronic Recoil Data from XENONnT, *Phys. Rev. Lett.* **129**, 161805 (2022), arXiv:2207.11330 [hep-ex].
 - [2] K. Bays *et al.* (Super-Kamiokande), Supernova Relic Neutrino Search at Super-Kamiokande, *Phys. Rev. D* **85**, 052007 (2012), arXiv:1111.5031 [hep-ex].
 - [3] C. Kachulis *et al.* (Super-Kamiokande), Search for Boosted Dark Matter Interacting With Electrons in Super-Kamiokande, *Phys. Rev. Lett.* **120**, 221301 (2018), arXiv:1711.05278 [hep-ex].
 - [4] J. A. Dror, G. Elor, R. McGehee, and T.-T. Yu, Absorption of sub-MeV fermionic dark matter by electron targets, *Phys. Rev. D* **103**, 035001 (2021), [Erratum: *Phys.Rev.D* 105, 119903 (2022)], arXiv:2011.01940 [hep-ph].
 - [5] J. A. Dror, G. Elor, and R. McGehee, Directly Detecting Signals from Absorption of Fermionic Dark Matter, *Phys. Rev. Lett.* **124**, 18 (2020), arXiv:1905.12635 [hep-ph].
 - [6] J. A. Dror, G. Elor, and R. McGehee, Absorption of Fermionic Dark Matter by Nuclear Targets, *JHEP* **02**, 134, arXiv:1908.10861 [hep-ph].
 - [7] T. Bringmann and M. Pospelov, Novel direct detection constraints on light dark matter, *Phys. Rev. Lett.* **122**, 171801 (2019), arXiv:1810.10543 [hep-ph].
 - [8] C. V. Cappiello, K. C. Y. Ng, and J. F. Beacom, Reverse Direct Detection: Cosmic Ray Scattering With Light Dark Matter, *Phys. Rev. D* **99**, 063004 (2019), arXiv:1810.07705 [hep-ph].
 - [9] C. V. Cappiello and J. F. Beacom, Erratum: Strong new limits on light dark matter from neutrino experiments [*Phys. Rev. D* 100, 103011 (2019)], *Phys. Rev. D* **100**, 103011 (2019), [Erratum: *Phys.Rev.D* 104, 069901 (2021)], arXiv:1906.11283 [hep-ph].
 - [10] Y. Ema, F. Sala, and R. Sato, Light Dark Matter at Neutrino Experiments, *Phys. Rev. Lett.* **122**, 181802 (2019), arXiv:1811.00520 [hep-ph].
 - [11] J. B. Dent, B. Dutta, J. L. Newstead, I. M. Shoemaker, and N. T. Arellano, Present and future status of light dark matter models from cosmic-ray electron upscattering, *Phys. Rev. D* **103**, 095015 (2021), arXiv:2010.09749 [hep-ph].
 - [12] Y. Jho, J.-C. Park, S. C. Park, and P.-Y. Tseng, Leptonic New Force and Cosmic-ray Boosted Dark Matter for the XENON1T Excess, *Phys. Lett. B* **811**, 135863 (2020), arXiv:2006.13910 [hep-ph].
 - [13] J. Bramante, B. J. Kavanagh, and N. Raj, Scattering searches for dark matter in subhalos: neutron stars, cosmic rays, and old rocks, (2021), arXiv:2109.04582 [hep-ph].
 - [14] Y. Farzan and S. Palomares-Ruiz, Dips in the Diffuse Supernova Neutrino Background, *JCAP* **06**, 014, arXiv:1401.7019 [hep-ph].

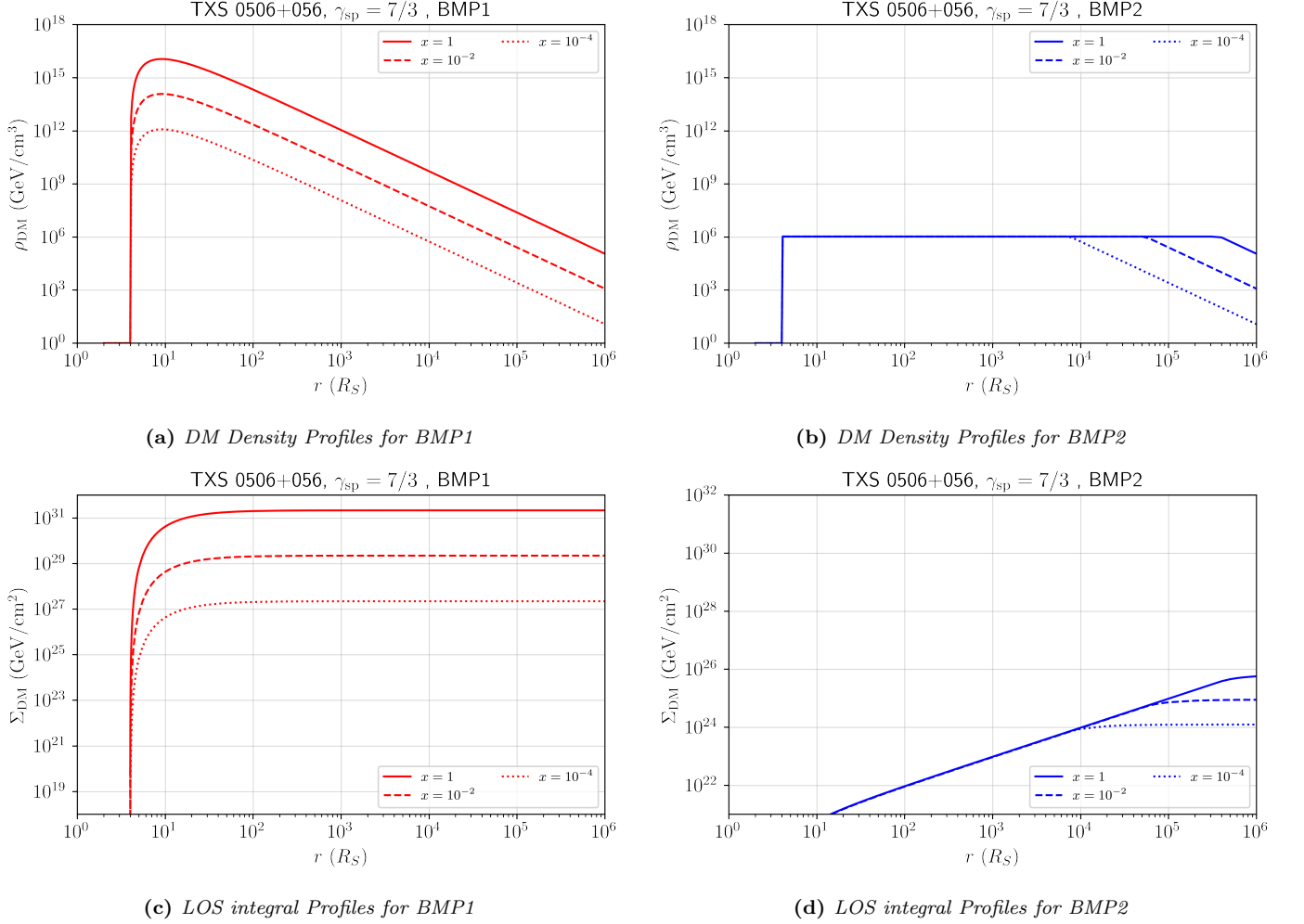


FIG. 9: The DM density profiles and LOS integral profiles for $\gamma_{sp} = 7/3$ are plotted above for BMP1 (red lines) and BMP2 (blue lines). The values of x chosen are $x = 1$ (solid lines), $x = 10^{-2}$ (dashed lines) and $x = 10^{-4}$ (dotted lines).

- [15] C. A. Argüelles, A. Kheirandish, and A. C. Vincent, Imaging Galactic Dark Matter with High-Energy Cosmic Neutrinos, *Phys. Rev. Lett.* **119**, 201801 (2017), arXiv:1703.00451 [hep-ph].
- [16] W. Yin, Highly-boosted dark matter and cutoff for cosmic-ray neutrinos through neutrino portal, *EPJ Web Conf.* **208**, 04003 (2019), arXiv:1809.08610 [hep-ph].
- [17] Y. Jho, J.-C. Park, S. C. Park, and P.-Y. Tseng, Cosmic-Neutrino-Boosted Dark Matter (ν BDM), (2021), arXiv:2101.11262 [hep-ph].
- [18] A. Das and M. Sen, Boosted dark matter from diffuse supernova neutrinos, (2021), arXiv:2104.00027 [hep-ph].
- [19] D. Ghosh, A. Guha, and D. Sachdeva, Exclusion limits on dark matter-neutrino scattering cross section, *Phys. Rev. D* **105**, 103029 (2022).
- [20] Q.-H. Cao, R. Ding, and Q.-F. Xiang, Searching for sub-MeV boosted dark matter from xenon electron direct detection, *Chin. Phys. C* **45**, 045002 (2021), arXiv:2006.12767 [hep-ph].
- [21] Y. Ema, F. Sala, and R. Sato, Neutrino experiments probe hadrophilic light dark matter, *SciPost Phys.* **10**, 072 (2021), arXiv:2011.01939 [hep-ph].
- [22] C. Xia, Y.-H. Xu, and Y.-F. Zhou, Azimuthal asymmetry in cosmic-ray boosted dark matter flux, (2022), arXiv:2206.11454 [hep-ph].
- [23] G. Elor, R. McGehee, and A. Pierce, Maximizing Direct Detection with HYPER Dark Matter, (2021), arXiv:2112.03920 [hep-ph].
- [24] T. N. Maity and R. Laha, Cosmic-ray boosted dark matter in Xe-based direct detection experiments, (2022), arXiv:2210.01815 [hep-ph].
- [25] R. Calabrese, M. Chianese, D. F. G. Fiorillo, and N. Saviano, Electron scattering of light new particles from evaporating primordial black holes, *Phys. Rev. D* **105**, 103024 (2022), arXiv:2203.17093 [hep-ph].
- [26] R. Calabrese, M. Chianese, D. F. G. Fiorillo, and N. Saviano, Direct detection of light dark matter from evaporating primordial black holes, *Phys. Rev. D* **105**, L021302 (2022), arXiv:2107.13001 [hep-ph].

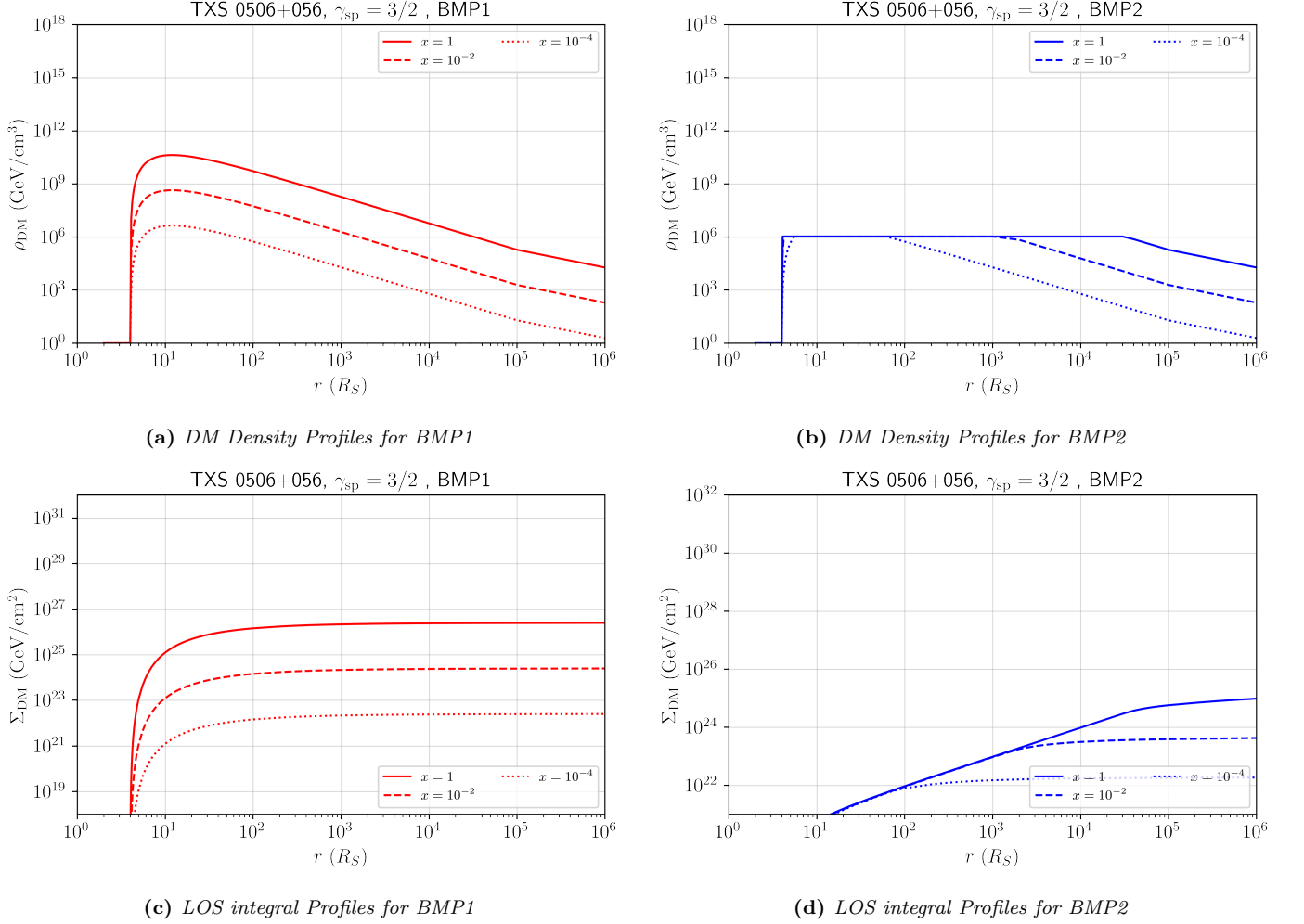


FIG. 10: The DM density profiles and LOS integral profiles for $\gamma_{sp} = 3/2$ are plotted above for BMP1 (red lines) and BMP2 (blue lines). The values of x chosen are $x = 1$ (solid lines), $x = 10^{-2}$ (dashed lines) and $x = 10^{-4}$ (dotted lines).

- [27] J.-W. Wang, A. Granelli, and P. Ullio, Direct Detection Constraints on Blazar-Boosted Dark Matter, *Phys. Rev. Lett.* **128**, 221104 (2022), arXiv:2111.13644 [astro-ph.HE].
- [28] A. Granelli, P. Ullio, and J.-W. Wang, Blazar-boosted dark matter at Super-Kamiokande, *JCAP* **07** (07), 013, arXiv:2202.07598 [astro-ph.HE].
- [29] J. B. Dent, B. Dutta, J. L. Newstead, and I. M. Shoemaker, Bounds on Cosmic Ray-Boosted Dark Matter in Simplified Models and its Corresponding Neutrino-Floor, *Phys. Rev. D* **101**, 116007 (2020), arXiv:1907.03782 [hep-ph].
- [30] A. A. Abdo *et al.*, The Spectral Energy Distribution of Fermi bright blazars, *Astrophys. J.* **716**, 30 (2010), arXiv:0912.2040 [astro-ph.CO].
- [31] A. Keivani *et al.*, A Multimessenger Picture of the Flaring Blazar TXS 0506+056: implications for High-Energy Neutrino Emission and Cosmic Ray Acceleration, *Astrophys. J.* **864**, 84 (2018), arXiv:1807.04537 [astro-ph.HE].
- [32] M. Cerruti, A. Zech, C. Boisson, G. Emery, S. Inoue, and J. P. Lenain, Leptohadronic single-zone models for the electromagnetic and neutrino emission of TXS 0506+056, *Mon. Not. Roy. Astron. Soc.* **483**, L12 (2019), [Erratum: *Mon. Not. Roy. Astron. Soc.* 502, L21–L22 (2021)], arXiv:1807.04335 [astro-ph.HE].
- [33] X. Rodrigues, S. Gao, A. Fedynitch, A. Palladino, and W. Winter, Leptohadronic Blazar Models Applied to the 2014–2015 Flare of TXS 0506+056, *Astrophys. J. Lett.* **874**, L29 (2019), arXiv:1812.05939 [astro-ph.HE].
- [34] R. Xue, R.-Y. Liu, M. Petropoulou, F. Oikonomou, Z.-R. Wang, K. Wang, and X.-Y. Wang, A two-zone model for blazar emission: implications for TXS 0506+056 and the neutrino event IceCube-170922A 10.3847/1538-4357/ab4b44 (2019), arXiv:1908.10190 [astro-ph.HE].
- [35] M. Petropoulou *et al.*, Multi-Epoch Modeling of TXS 0506+056 and Implications for Long-Term High-Energy Neutrino Emission, *Astrophys. J.* **891**, 115 (2020), arXiv:1911.04010 [astro-ph.HE].
- [36] M. G. Aartsen *et al.* (IceCube, Fermi-LAT, MAGIC, AGILE, ASAS-SN, HAWC, H.E.S.S., INTEGRAL, Kanata, Kiso, Kapteyn, Liverpool Telescope, Subaru, Swift NuSTAR, VERITAS, VLA/17B-403), Multimessenger observations of a flaring blazar coincident with high-energy neutrino IceCube-170922A, *Science* **361**, eaat1378 (2018), arXiv:1807.08816

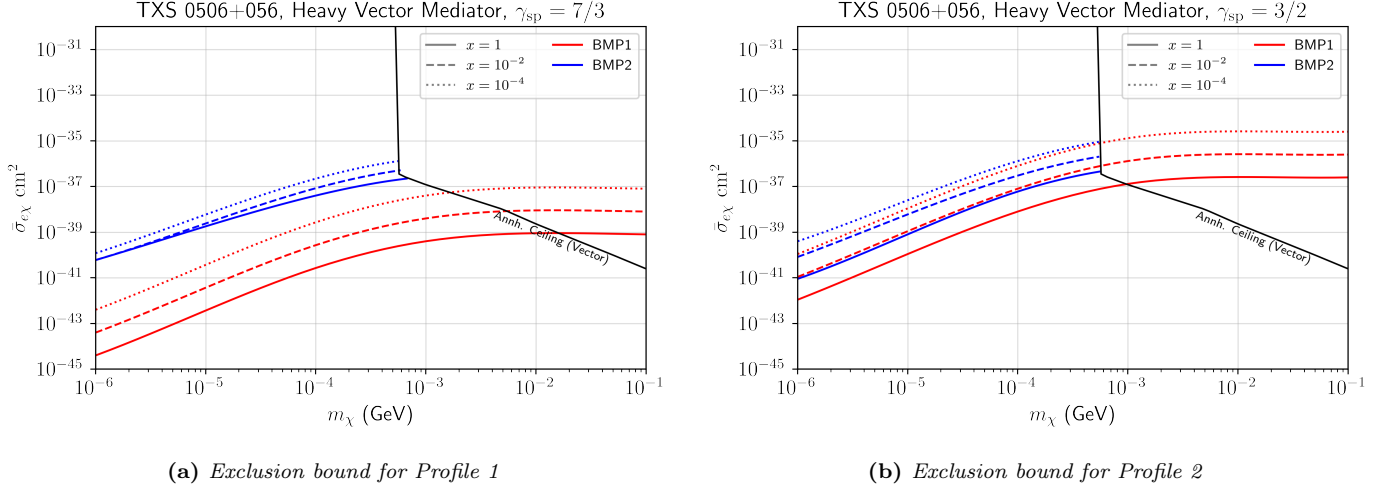


FIG. 11: The exclusion bound is plotted for the blazar TXS 0506+056 for BMP1 (red lines) and BMP2 (blue lines), corresponding to the heavy vector mediator scenario, for $\gamma_{sp} = 7/3$ (11a) and $\gamma_{sp} = 3/2$ (11b). The values of x chosen are $x = 1$ (solid lines), $x = 10^{-2}$ (dashed lines) and $x = 10^{-4}$ (dotted lines).

[astro-ph.HE].

- [37] M. G. Aartsen *et al.* (IceCube), Neutrino emission from the direction of the blazar TXS 0506+056 prior to the IceCube-170922A alert, *Science* **361**, 147 (2018), arXiv:1807.08794 [astro-ph.HE].
- [38] P. Padovani, P. Giommi, E. Resconi, T. Glauch, B. Arsioli, N. Sahakyan, and M. Huber, Dissecting the region around IceCube-170922A: the blazar TXS 0506+056 as the first cosmic neutrino source, *Mon. Not. Roy. Astron. Soc.* **480**, 192 (2018), arXiv:1807.04461 [astro-ph.HE].
- [39] C. D. Dermer and G. Menon, *High Energy Radiation from Black Holes: Gamma Rays, Cosmic Rays, and Neutrinos* (Princeton University Press, 2009).
- [40] M. Gorchtein, S. Profumo, and L. Ubaldi, Probing Dark Matter with AGN Jets, *Phys. Rev. D* **82**, 083514 (2010), [Erratum: *Phys.Rev.D* 84, 069903 (2011)], arXiv:1008.2230 [astro-ph.HE].
- [41] M. Boettcher, A. Reimer, K. Sweeney, and A. Prakash, Leptonic and Hadronic Modeling of Fermi-Detected Blazars, *Astrophys. J.* **768**, 54 (2013), arXiv:1304.0605 [astro-ph.HE].
- [42] P. Gondolo and J. Silk, Dark matter annihilation at the galactic center, *Phys. Rev. Lett.* **83**, 1719 (1999), arXiv:astro-ph/9906391.
- [43] P. Ullio, H. Zhao, and M. Kamionkowski, A Dark matter spike at the galactic center?, *Phys. Rev. D* **64**, 043504 (2001), arXiv:astro-ph/0101481.
- [44] G. Bertone and D. Merritt, Time-dependent models for dark matter at the Galactic Center, *Phys. Rev. D* **72**, 103502 (2005), arXiv:astro-ph/0501555.
- [45] M. Pospelov, A. Ritz, and M. B. Voloshin, Secluded WIMP Dark Matter, *Phys. Lett. B* **662**, 53 (2008), arXiv:0711.4866 [hep-ph].
- [46] B. Batell, M. Pospelov, and A. Ritz, Exploring Portals to a Hidden Sector Through Fixed Targets, *Phys. Rev. D* **80**, 095024 (2009), arXiv:0906.5614 [hep-ph].
- [47] X. Chu, T. Hambye, and M. H. G. Tytgat, The Four Basic Ways of Creating Dark Matter Through a Portal, *JCAP* **05**, 034, arXiv:1112.0493 [hep-ph].
- [48] A. Alves, S. Profumo, and F. S. Queiroz, The dark Z' portal: direct, indirect and collider searches, *JHEP* **04**, 063, arXiv:1312.5281 [hep-ph].
- [49] E. Izaguirre, G. Krnjaic, P. Schuster, and N. Toro, New Electron Beam-Dump Experiments to Search for MeV to few-GeV Dark Matter, *Phys. Rev. D* **88**, 114015 (2013), arXiv:1307.6554 [hep-ph].
- [50] E. Izaguirre, G. Krnjaic, P. Schuster, and N. Toro, Analyzing the Discovery Potential for Light Dark Matter, *Phys. Rev. Lett.* **115**, 251301 (2015), arXiv:1505.00011 [hep-ph].
- [51] G. Krnjaic, Probing Light Thermal Dark-Matter With a Higgs Portal Mediator, *Phys. Rev. D* **94**, 073009 (2016), arXiv:1512.04119 [hep-ph].
- [52] E. Izaguirre, Y. Kahn, G. Krnjaic, and M. Moschella, Testing Light Dark Matter Coannihilation With Fixed-Target Experiments, *Phys. Rev. D* **96**, 055007 (2017), arXiv:1703.06881 [hep-ph].
- [53] K. Harigaya, R. McGehee, H. Murayama, and K. Schutz, A predictive mirror twin Higgs with small Z_2 breaking, *JHEP* **05**, 155, arXiv:1905.08798 [hep-ph].
- [54] E. Bernreuther, S. Heeba, and F. Kahlhoefer, Resonant sub-GeV Dirac dark matter, *JCAP* **03**, 040, arXiv:2010.14522 [hep-ph].
- [55] P. A. Zyla *et al.* (Particle Data Group), Review of Particle Physics, *PTEP* **2020**, 083C01 (2020).

- [56] R. Essig, A. Manalaysay, J. Mardon, P. Sorensen, and T. Volansky, First Direct Detection Limits on sub-GeV Dark Matter from XENON10, *Phys. Rev. Lett.* **109**, 021301 (2012), arXiv:1206.2644 [astro-ph.CO].
- [57] R. Essig, T. Volansky, and T.-T. Yu, New Constraints and Prospects for sub-GeV Dark Matter Scattering off Electrons in Xenon, *Phys. Rev. D* **96**, 043017 (2017), arXiv:1703.00910 [hep-ph].
- [58] L. Barak *et al.* (SENSEI), SENSEI: Direct-Detection Results on sub-GeV Dark Matter from a New Skipper-CCD, *Phys. Rev. Lett.* **125**, 171802 (2020), arXiv:2004.11378 [astro-ph.CO].
- [59] P. Agnes *et al.* (DarkSide-50), Search for dark matter particle interactions with electron final states with DarkSide-50, (2022), arXiv:2207.11968 [hep-ex].
- [60] H. An, M. Pospelov, J. Pradler, and A. Ritz, Directly Detecting MeV-scale Dark Matter via Solar Reflection, *Phys. Rev. Lett.* **120**, 141801 (2018), [Erratum: *Phys.Rev.Lett.* 121, 259903 (2018)], arXiv:1708.03642 [hep-ph].
- [61] D. Bardhan, S. Bhowmick, D. Ghosh, A. Guha, and D. Sachdeva, Boosting through the Darkness : Bounds on boosted dark matter from direct detection, (2022), arXiv:2208.09405 [hep-ph].
- [62] K. Petraki and R. R. Volkas, Review of asymmetric dark matter, *Int. J. Mod. Phys. A* **28**, 1330028 (2013), arXiv:1305.4939 [hep-ph].
- [63] Y. Hochberg, I. Charaev, S.-W. Nam, V. Verma, M. Colangelo, and K. K. Berggren, Detecting Sub-GeV Dark Matter with Superconducting Nanowires, *Phys. Rev. Lett.* **123**, 151802 (2019), arXiv:1903.05101 [hep-ph].
- [64] Y. Hochberg, B. V. Lehmann, I. Charaev, J. Chiles, M. Colangelo, S. W. Nam, and K. K. Berggren, New Constraints on Dark Matter from Superconducting Nanowires, (2021), arXiv:2110.01586 [hep-ph].
- [65] Y. M. Andreev *et al.*, Improved exclusion limit for light dark matter from e^+e^- annihilation in NA64, *Phys. Rev. D* **104**, L091701 (2021), arXiv:2108.04195 [hep-ex].
- [66] J. P. Lees *et al.* (BaBar), Search for Invisible Decays of a Dark Photon Produced in e^+e^- Collisions at BaBar, *Phys. Rev. Lett.* **119**, 131804 (2017), arXiv:1702.03327 [hep-ex].
- [67] S. Knapen, T. Lin, and K. M. Zurek, Light Dark Matter: Models and Constraints, *Phys. Rev. D* **96**, 115021 (2017), arXiv:1709.07882 [hep-ph].
- [68] D. Ghosh and D. Sachdeva, Constraints on Axion-Lepton coupling from Big Bang Nucleosynthesis, *JCAP* **10**, 060, arXiv:2007.01873 [hep-ph].
- [69] M. Escudero, Neutrino decoupling beyond the Standard Model: CMB constraints on the Dark Matter mass with a fast and precise N_{eff} evaluation, *JCAP* **02**, 007, arXiv:1812.05605 [hep-ph].
- [70] N. Aghanim *et al.* (Planck), Planck 2018 results. VI. Cosmological parameters, *Astron. Astrophys.* **641**, A6 (2020), [Erratum: *Astron.Astrophys.* 652, C4 (2021)], arXiv:1807.06209 [astro-ph.CO].
- [71] D. Choudhury, S. Maharana, D. Sachdeva, and V. Sahdev, Dark matter, muon anomalous magnetic moment, and the XENON1T excess, *Phys. Rev. D* **103**, 015006 (2021), arXiv:2007.08205 [hep-ph].
- [72] J. M. Cline, S. Gao, F. Guo, Z. Lin, S. Liu, M. Puel, P. Todd, and T. Xiao, Blazar constraints on neutrino-dark matter scattering, (2022), arXiv:2209.02713 [hep-ph].